Supporting information for

Synergy of coordination and trace ionization from co-solvents enables reversible magnesium electroplating/stripping behavior

Min Wang[1], Wenhao Sun[1], Kun Zhang[4], Zhonghua Zhang[*1,3], Aobing Du[3], Shanmu Dong[3], Jinlei Zhang [1], Jing Liu[1,2], Xi Chen[5], Zhenfang Zhou, Fujun Li[6], Zhenjiang Li[1], Guicun Li[*1] and Guanglei Cui[*3]

1 College of Materials Science and Engineering, Qingdao University of Science and Technology, Qingdao 266042, P. R. China.

2 Department of Pharmacy, Jining Medical University, Rizhao 276826, P. R. China.

3 Qingdao Industrial Energy Storage Research Institute, Qingdao Institute of Bioenergy and Bioprocess Technology, Chinese Academy of Sciences, Qingdao 266101, P. R. China.

4 Zibo Institute for Product Quality Inspection, Zibo 255063, P. R. China.

5 Department of Physics, Xi'an Jiaotong-Liverpool University, Suzhou 215123, P. R. China.

6 Key Laboratory of Advanced Energy Materials Chemistry (Ministry of Education), Nankai University, Tianjin 300071, P. R. China.

*Corresponding authors: zhangzh@qust.edu.cn; guicunli@qust.edu.cn; cuigl@qibebt.ac.cn

This profile contains *Experimental section*, *Figure S1-S29, Table S1-S4 and corresponding discussions*.

1. Experimental section

1.1 Experimental materials

$Mg(TFSI)_2$ (99.5%, Solvionic), diethylene glycol dimethyl ether (G2, 99.5%, Sigma-Aldrich), tetrahydrofuran (THF, 99.9%, Sigma-Aldrich), 3-dimethylaminopopylamine (DMAPA, 99%, Macklin), isobutylamine (IBA, 99.5%, Energy Chemical), o-toluidine (OT, 99.5%, Macklin), dimethylamine solution (DMA, 2.0 M solution in THF, Macklin), bis(2-methoxyethyl) (BMA, 98%, Aladdin), triethylamine (TEA, 99.5%, Macklin), tripropylamine (TPA, 99%, Macklin) are used as received without further treatment.

1.2 Electrolyte preparation

$Mg(TFSI)_2$ was dissolved in the mixed solution of G2-DMAPA and stirred continuously for 1 h to keep the Mg ion concentration at 0.1 M. The mixed solution of G2-DMAPA should be stirred for 10 min before use to ensure that the mixture could be fully dissolved. Similar methods were used to prepare electrolyte containing (DMAPA, DMA, IBA, OT, BMA, TEA, TPA. The mass ratio of mixed solution composition was G2/DMAPA=4.04/1, G2/DMA=6.2/1, G2/IBA=9.5/1, G2/BMA=4.0/1, G2/OT=6.3/1, G2/TEA=4.0/1, G2/TPA=4.2/1. Dissolve the Mg(TFSI)2 salt into the solvent mixture. All experimental operations were carried out in the Ar-filled glove box (H_2O, $O_2 < 0.1$ ppm).

1.3 Battery assembly and electrochemical performance tests

All batteries were assembled in 2032-type cells in Ar-filled glove box. The asymmetric Mg//Cu or Mg//SS cells were composed of Mg foil (0.1 mm in thickness, Beijing Juguang Technology Co, LTD.), Cu foil (0.9 mm in thickness, Beijing Gaoke New Material Co, LTD.) or SS (stainless steel) foil (0.01 mm, 316), GF separator (GF/D, Whatman) and PI separator. 180 μL electrolyte was dropped onto the GF separator. The cells were assembled with a Compact Crimping Machine (MSK-160E, HEFEI KEJING MATERIALS TECHNOLGY CO, LTD.) at 1T pressure. All batteries were allowed to stand for 12 h before the LAND battery test system (CT2001A and CT3002A).

CV measurements were performed on electrochemical workstation (Autolab PGSTAT302N) at a scan rate of 25 (or 10) mV s^{-1} over a voltage range of -1.0 V to 2.0 V relative to Mg/Mg^{2+}. EIS and LSV tests were performed on the same electrochemical workstation.

The ionic conductivities of electrolytes were tested by EIS. Two SS foils were used as two symmetrical electrodes and glass fiber was used as separator. The assembled battery was aged for 12 h. The test frequency was selected from 1000 Hz to 10 mHz, and the disturbance voltage was set at 10.0 mV.

1.4 Structural investigation on electrodeposits

The scanning electron microscope (SEM) was used to photograph the sample morphology and energy spectrum mapping on TESCAN MIRA LMS equipment. A small piece of PI with the electroplating product is directly glued to the conductive adhesive. The Oxford Quorum SC7620 sputtering coater is used to spray gold for 45 s.

X-ray diffraction (XRD) characterizations were performed with D/MAX/2500PC X-ray diffraction. The test range is 20-70°. The light source is Cu-Kα ray.

X-ray photoelectron spectroscopy (XPS) characterizations were performed with PHI5000 VersaprobeIII XPS (Mono Al Kα, 1486.6 eV, 15 kV, 4.5 mA, CAE mode).

Cryogenic electron microscopy (Cryo-EM) tests were performed with a Talos 200X TEM under ultra-low temperature of about 95K and operated at 200 kV. All TEM images were obtained with a Ceta camera. STEM images were obtained with HAADF detector, and EDS tests were operated with SuperX energy dispersive spectroscopy. Conventional transmission electron microscopy (TEM) characterizations were performed with JEM-2100PLUS and JEOL JEM-F200 transmission electron microscopes.

Time-of-flight secondary ion mass spectrometry was performed with a TOF-SIMS (TOF-SIMS 5 iontof，Germany).

Titration experiments of MgH_2 were performed using a home-made on-line DEMS system[1]. The Mg//Cu cells with E-DAMPA electrolyte after different cycles were carefully disassembled in an Ar-filled glovebox with H_2O and O_2 content less than 0.1 ppm. The cycled Cu electrodes were carefully rinsed with dimethoxyethane (DME, aiming to exclude the effects of lithium salts), dried, weighed and well-sealed in the container of the titration unit. It was noted that, every time,

the components of the titration unit were washed with anhydrous alcohol and acetone for several times and dried at 80℃ for 12 hours under vacuum conditions. After connecting the sample-containing titration unit, the Ar carrier gas was switched to go through the titration unit, then 1 ml D_2O was injected. The amount of each gas was determined by plotting the processed data and integrating the peak area exclude the baseline. Then, the mole of D_2, HD and the corresponding mole of Mg, MgH_2 were calculated.

1.5 Electrolyte solution characterizations

^1H NMR characterization was performed on the NMR spectrometer (AVANCE-Ⅲ 600 MHz), A coaxial NMR tube was used to preserve the samples, and DMSO (99.9%, Sigma Aldrich) was placed sealed in an external NMR tube as a reference for ^1H NMR to lock the magnetic field during characterization.

A single crystal was chosen to collect diffraction data from the crystal. The slightly wet crystal was rapidly transferred to a cold N_2 stream on the instrument. The measurements were performed on a Bruker Smart Photon III detector using Mo radiation at 170 K. The structure was calculated and refined using Olex2 and Diamond 4 software. The crystallographic data and structure refinement are shown in **Table S1.**

FTIR characterization was performed on a Thermo Scientific Nicolet iS10 device.

Electrospray ionization-mass spectrometry (ESI-MS) test has been conducted using Thermo Scientific Q Exactive (ion source: HESI; warping rate: 40 mL/min; auxiliary gas rate: 10 mL/min; spray voltage: positive ions 3.0 kV, negative ions 2.5 kV; capillary temperature: 300 °C).

1.6 Electrostatic potential

Molecular surface electrostatic potential calculation using Material Studio software's DMol3[2] module, geometry optimizations and energy calculations were performed using B3LYP[3], Electron density and Electrostatics are checked in the properties option, Other parameters take default parameters. After the calculation, choose Electron density to output the electron density map, and electrostatics to output the electrostatic potential.

1.7 Gibbs free energy

The reaction equation for the Gibbs free energy change is shown in equation (1)

$$A+B\rightarrow C+D \tag{1}$$

Firstly, thermodynamic analysis is carried out to optimize the structures of reactants and products respectively using Material Studio software and calculate their Gibbs free energies. Then the Gibbs free energy change for this reaction is calculated from equation (2). Simulate the ΔrG of this reaction at 298.15 K, standard atmospheric pressure.

$$\Delta G=G_C+G_D-G_A-G_B \tag{2}$$

$$G=E_{sp}+G_T \tag{3}$$

The reactant and product Gibbs free energies can be calculated using equation (3). Here, GT is the temperature correction value, which can be obtained after structure optimization calculations for reactant or product molecules, and Esp is the single-point energy, which is the energy correction after optimizing the structure of the molecule with a higher precision method and basis group.

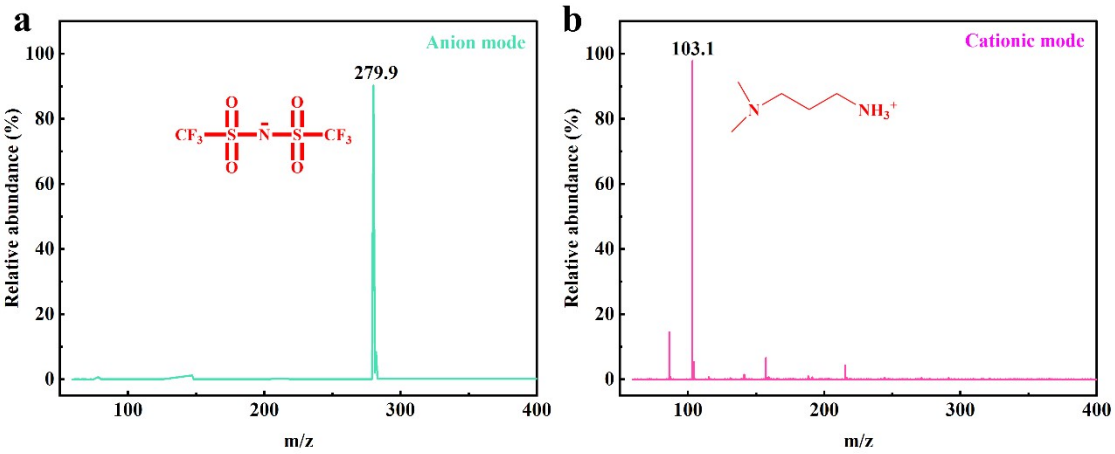

Figure S1. ESI-MS results of $Mg(TFSI)_2$/(G2+DMAPA)(a) electrolyte and G2+DMAPA co-solvent(b).

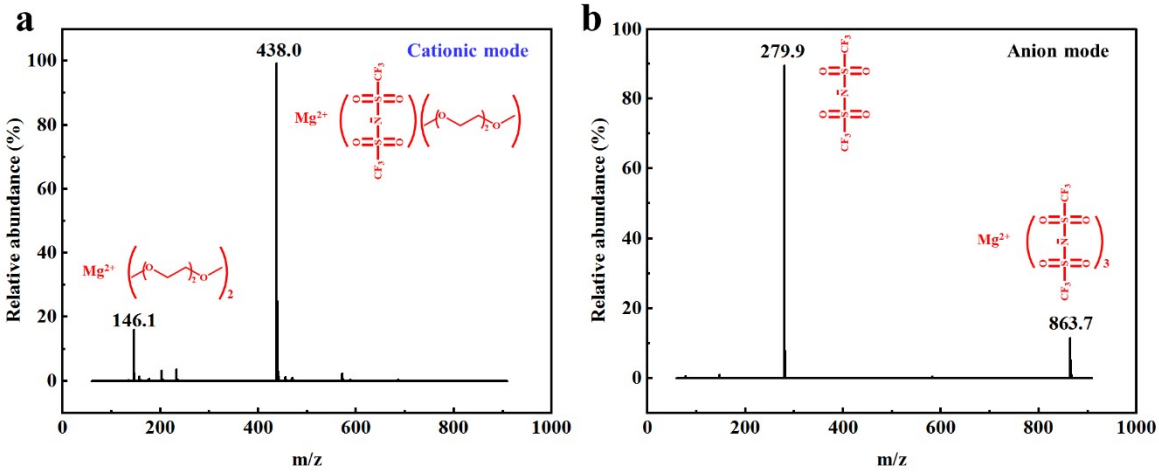

Figure S2. Mass spectra of 0.1 M $Mg(TFSI)_2$/G2 electrolyte. Cationic mode (a) and anion mode (b) in the 60-900 m/z region.

The results of electrospray ionization-mass spectrometry (ESI-MS) of $Mg(TFSI)_2$/G2 electrolyte showed the presence of two cation species, namely $[Mg(G2)_2]^{2+}$ and $[Mg(G2)(TFSI^-)]^+$, and the presence of $TFSI^-$ and $[Mg(TFSI^-)_3]^-$ in the anion mode.

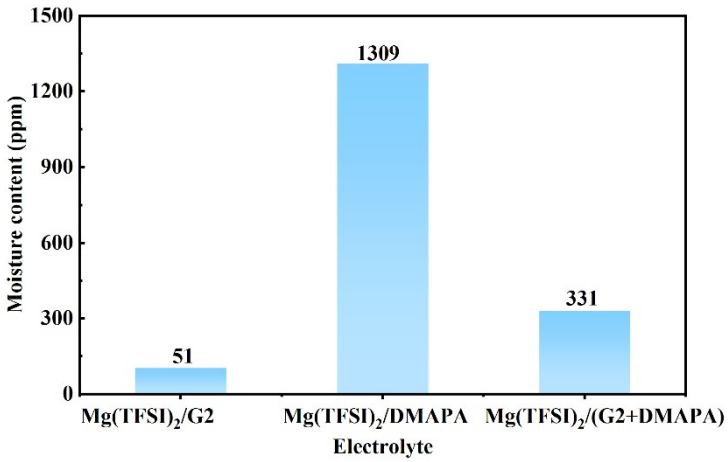

Figure S3. The moisture contents of the different electrolytes were determined using a Karl Fischer tests.

Figure S4: Optical photo of Mg foils immersed in various electrolytes and solvents. All experiments were conducted at a constant temperature of 30 °C.

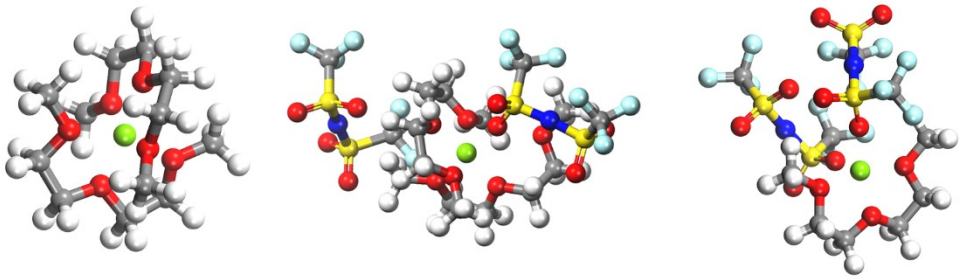

Figure S5. The optimized solvation structures obtained from MD simulation of 0.1 M $Mg(TFSI)_2$/G2 electrolyte. The partial relative binding energy are also shown.

The binding energies were calculated using DFT with the Forcite module in Materials Studio. The geometries were optimized and energy calculations were performed using the smart algorithm, with a maximum of 5000 iterations. COMPASS force field[4] was employed, and the force field charge was set to "Use Current". The Material Studio software package was used for all DFT calculations.
E(binding)=E(AB)-E(A)-E(B)

The relatively higher binding energy of $[Mg(G2)_2(TFSI^-)_2]^0$, $[Mg(G2)(TFSI^-)_2]^0$ might suggest the instability of these species in electrolyte.

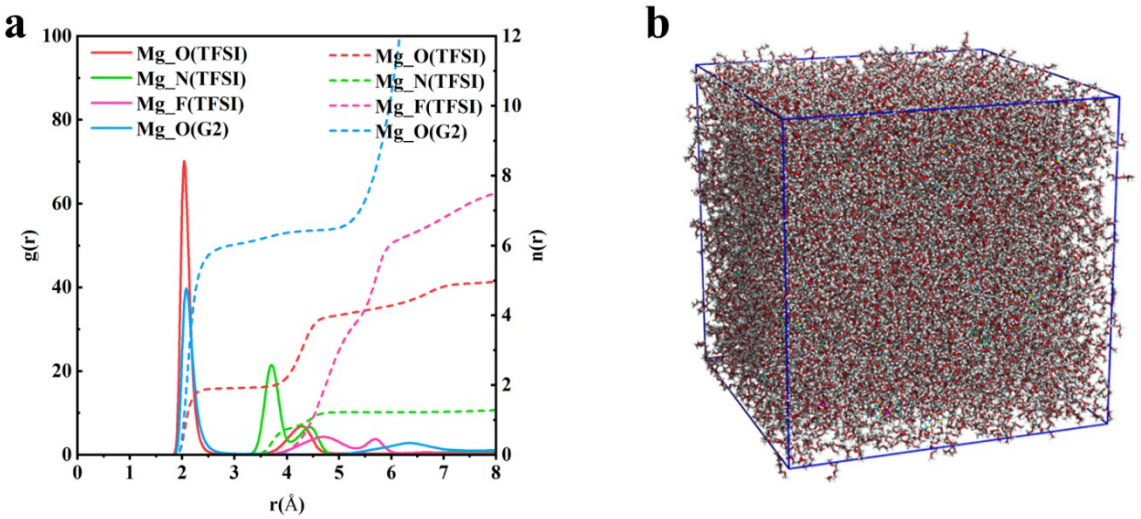

Figure S6. (a) RDF patterns of 0.1 M $Mg(TFSI)_2$/G2 electrolyte. (b) The corresponding snapshots of MD simulation results.

The 0.1 M $Mg(TFSI)_2$/G2 electrolyte system was also established by MD simulations. The RDF patterns show that the interaction between Mg^{2+} and TFSI anion (Mg_O (TFSI)) is more strong than that between Mg^{2+} and G2 molecule (Mg_O (G2)). The average coordination number of G2 molecule is six, while the average coordination number of TFSI anions is two. This indicates that Mg ions are mainly coordinated with TFSI anions and O of G2 molecules in this electrolyte system.

Quantum chemistry calculations were first performed to optimize molecular geometries of solvent molecules using the Gaussian 16 package[5] at B3LYP/6-311+G(d) level of theory. The atomistic force field parameters for all ions and molecules are described by the AMBER format and are taken from previous work[6]. A representative atomistic modelling system consisting of 100 $Mg(TFSI)_2$ ion pairs, 5550 G2 solvent molecules was constructed. Atomistic simulations of this modelling system were performed using GROMACS package with cubic periodic boundary conditions[7]. The particle-mesh Ewald (PME) summation method with an interpolation order of 5 and a Fourier grid spacing of 0.15 nm was employed to handle long range electrostatic interactions in reciprocal space. All simulation systems were first energetically minimized using a steepest descent algorithm, and thereafter annealed gradually from 700 K to room temperature (300 K) within 15 ns.

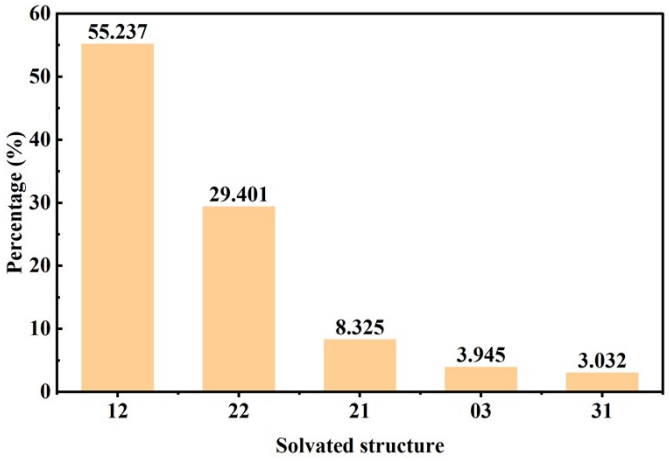

Figure S7. Statistical result of 100 complex structures from MD simulation of 0.1 M $Mg(TFSI)_2$/G2 electrolyte. Two consecutive numbers in abscissa indicate the complex structures of Mg-ion or Mg-anion ion-pairs. (e.g. 12 presents the Mg-anion ion-pairs consists of one TFSI anions, two G2 molecule).

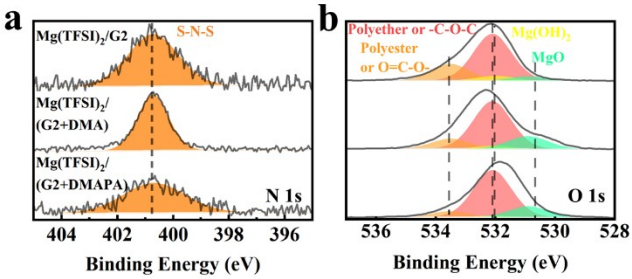

Figure S8. High-resolution N *1s* (a), and O *1s* (b) XPS spectra of electrodeposits. The S–N–S peaks observed is ascribed to the decomposition from TFSI anion. The –C–O–C and O=C–O– organic products might be from decomposition of G2 solvent in the electrolyte.

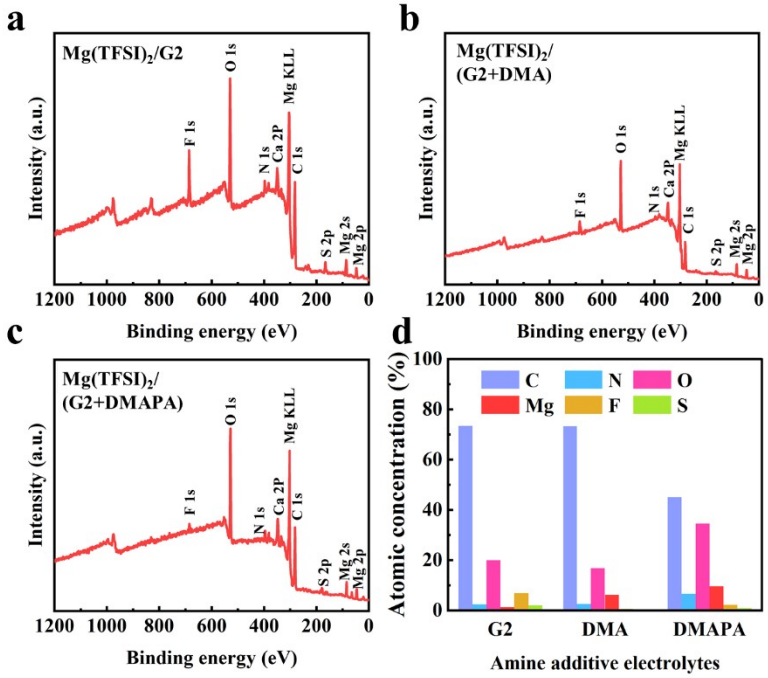

Figure S9. XPS characterization of electrodeposited products. (a) XPS survey of various electrolytes. (b) Corresponding atomic concentration.

As shown in **Figure S9d**. the comparison of the elemental content of XPS shows that the $Mg(TFSI)_2$/G2 electrolyte is dominated by the elemental content of C (73.44%), while the elemental content of Mg is minimal. However, for the other electrolytes with the introduction of amine solvents, the Mg content was increased to different degrees and the other elements such as C, F and S were decreased to different degrees. the increase of O content was mainly due to the higher sensitivity of Mg itself to water oxygen. The comparison of the elemental content further indicates that a weak passivation interlayer is formed in the $Mg(TFSI)_2$/(G2+DMAPA) electrolyte.

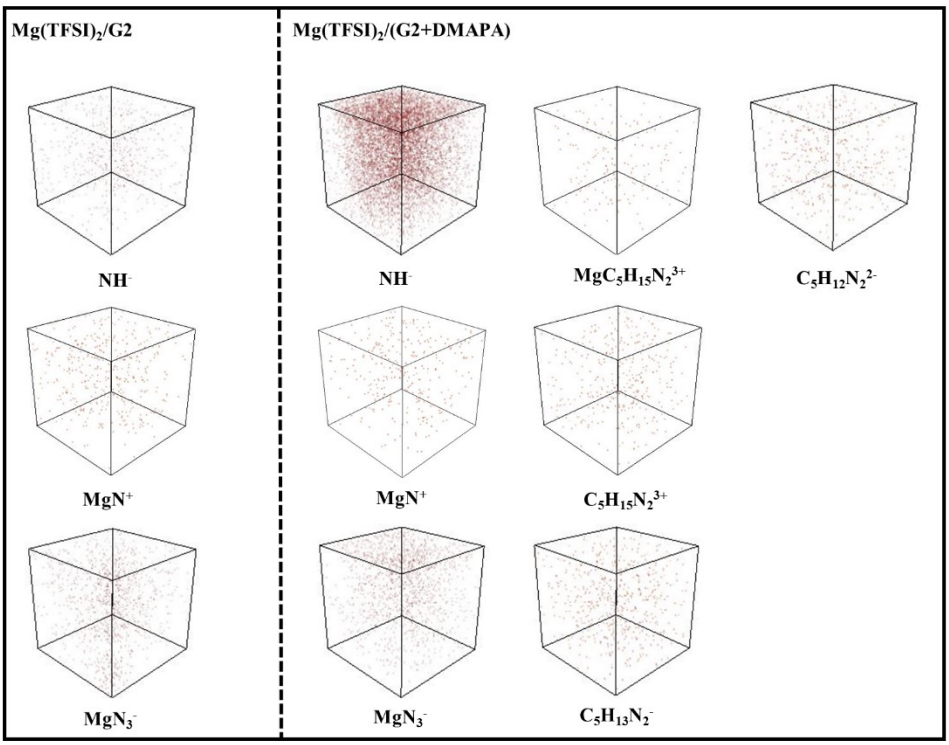

Figure S10. TOF-SIMS spectra of Mg//Mg cells for NH^-, MgN^+, MgN_3^-, $MgC_5H_{15}N_2^{3+}$, $C_5H_{15}N_2^{3+}$, $C_5H_{13}N_2^-$, and $C_5H_{12}N_2^{2-}$ after 20 cycles.

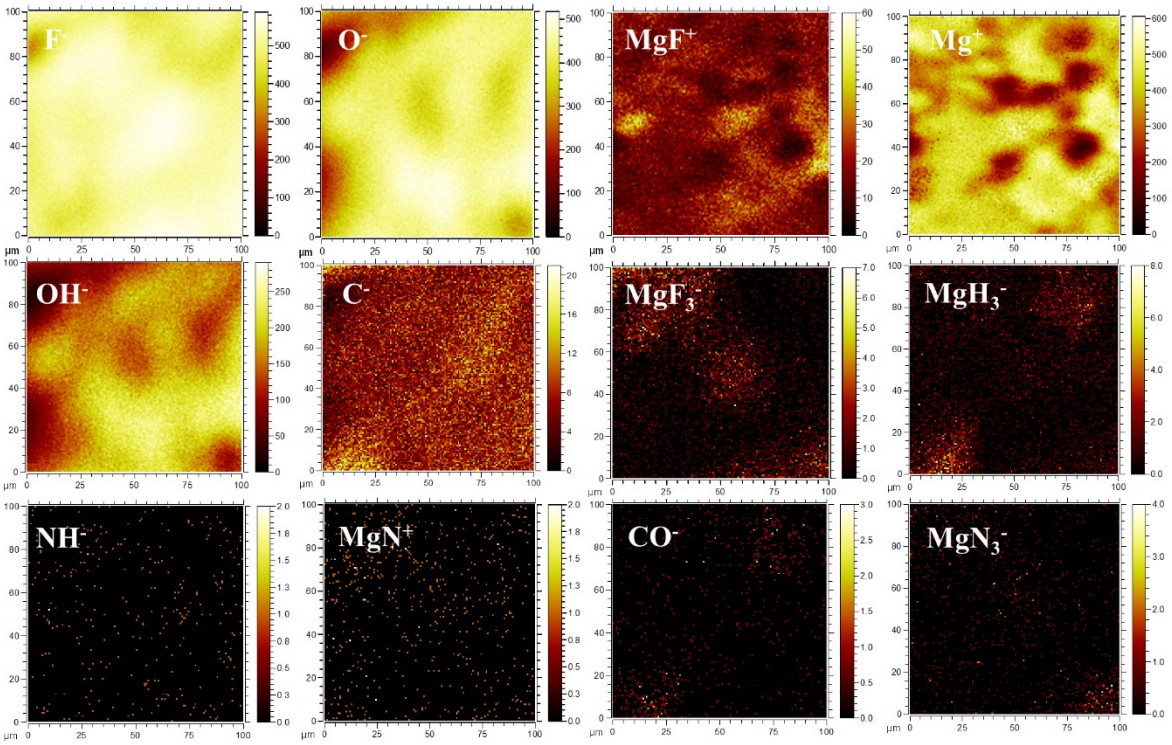

Figure S11. TOF-SIMS depth profiles show the distribution of various components on the surface of Mg//Mg cells in the $Mg(TFSI)_2$/G2 electrolyte after 20 cycles.

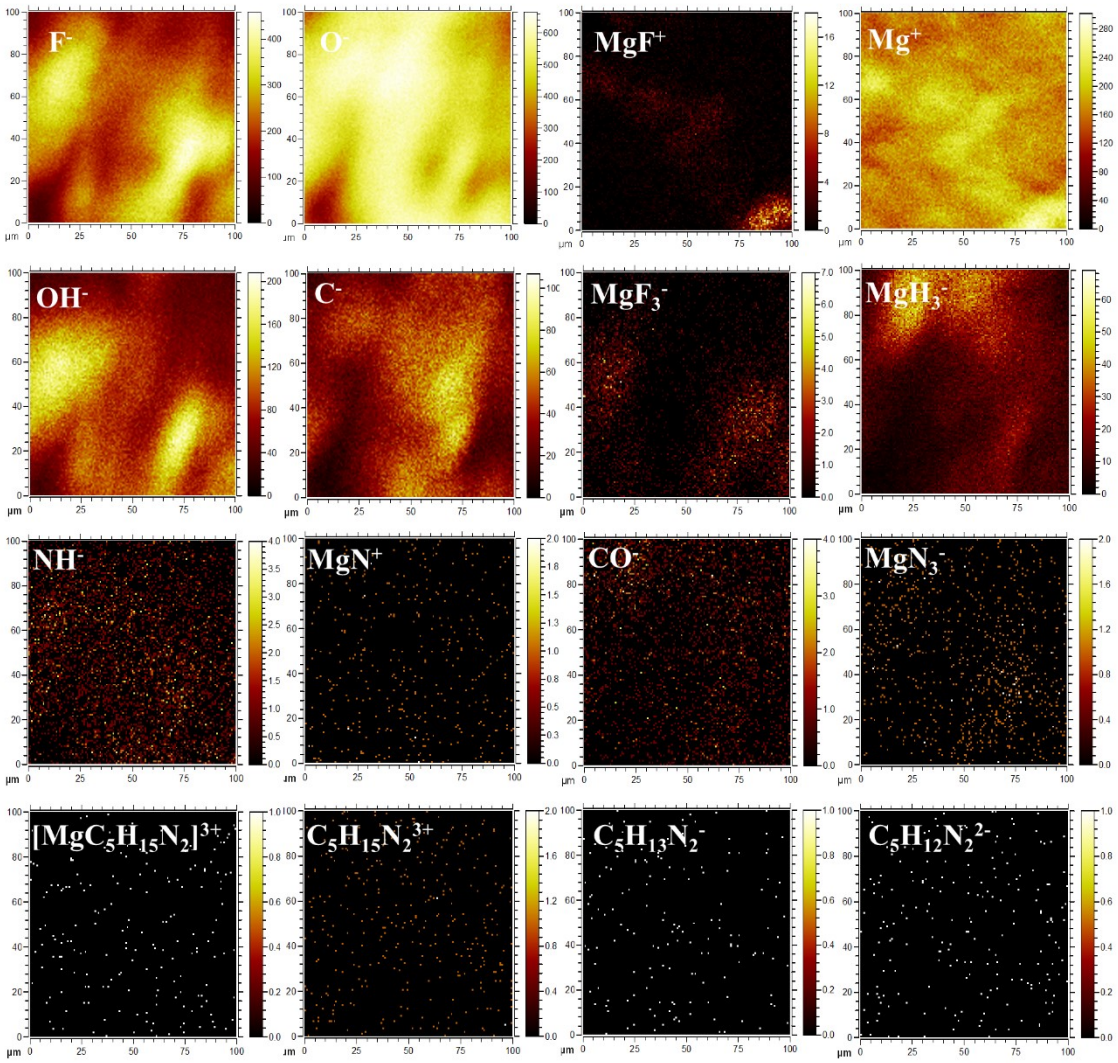

Figure S12. TOF-SIMS depth profiles show the distribution of various components on the surface of Mg//Mg cells in the $Mg(TFSI)_2$/(G2+DMAPA) electrolyte after 20 cycles.

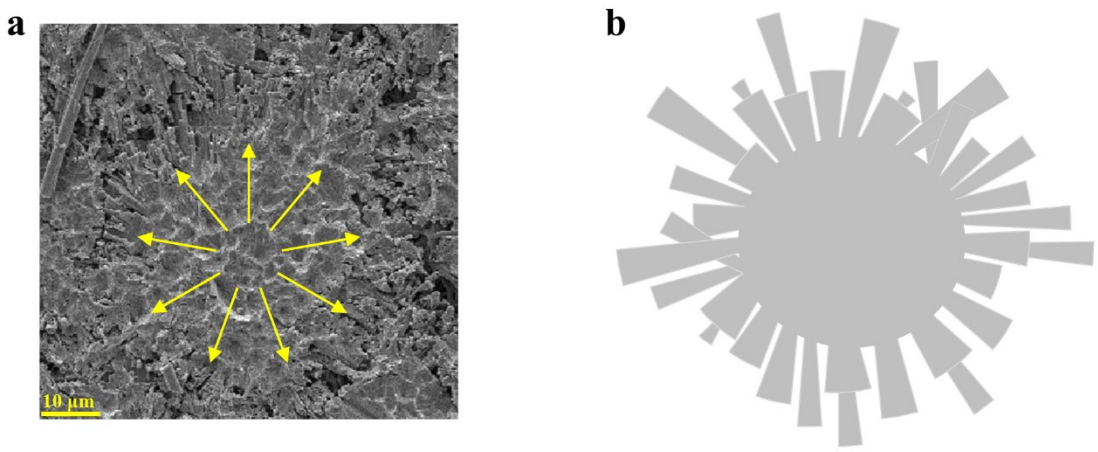

Figure S13. SEM images (a) and schematic diagram (b) of the radial growth traces of aggregated electrodeposition attached to the PI septum.

The growth traces of the aggregated electrodeposits can be clearly observed in the images, and this tiled prismatic radial Mg growth process is well represented, which indicates the continuous nucleation and growth of the electrodeposits. Due to this simple dispersive radial growth, a relatively smooth Mg microcrystalline aggregate is formed.

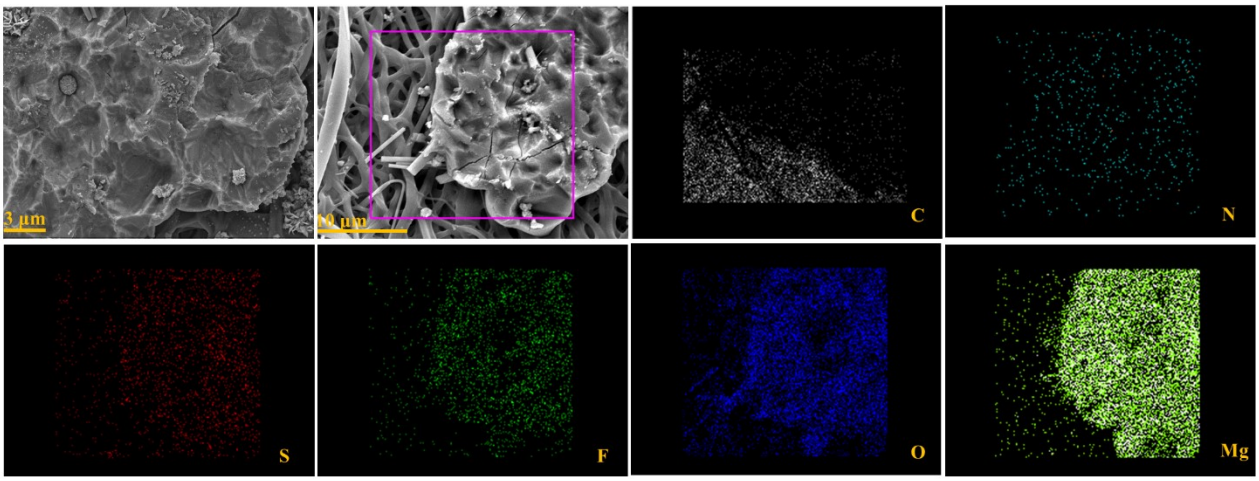

Figure S14. Typical SEM images of Mg planting on PI (Polyimide) substrates containing 0.1 M $Mg(TFSI)_2$/(G2+DMA) electrolyte, and corresponding mapping of various elements EDS elements (scale bars: 10µm).

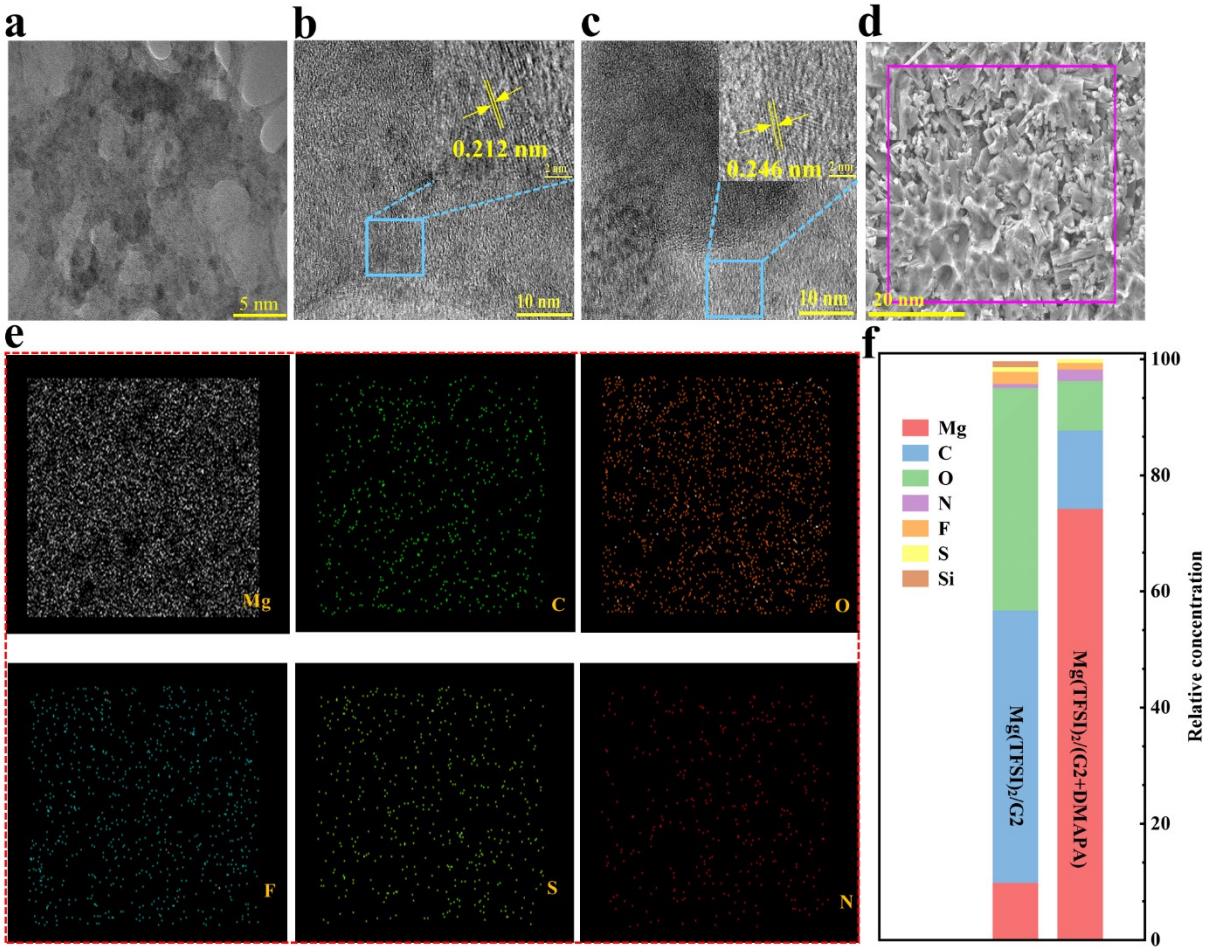

Figure S15. Characterization of Mg deposition products. (a) TEM image of the deposition product. (b-c) TEM and HRTEM image of electrodepositions from 0.1 M $Mg(TFSI)_2$/(G2+DMAPA) electrolyte after 10 hours discharging at 0.1 mAh cm^{-2}. (d-e) STEM-EDS mappings analysis of the deposits (f) Molar rate of decomposition of the electrodeposited products of $Mg(TFSI)_2$/G2 and $Mg(TFSI)_2$/(G2+DMAPA) electrolytes.

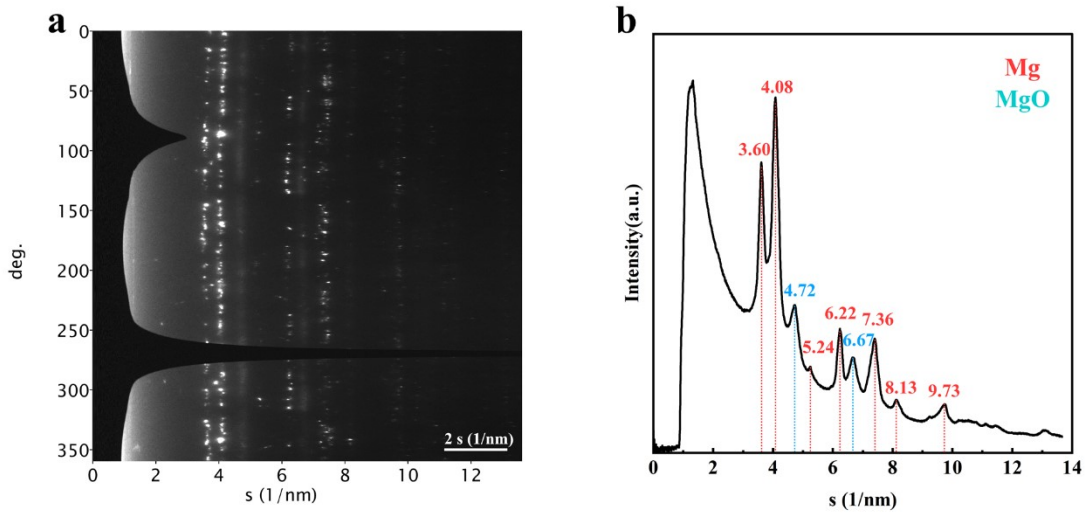

Figure S16. Linear image (a) and intensity profile (b) of SAED patterns for Mg and MgO in Figure 4f.

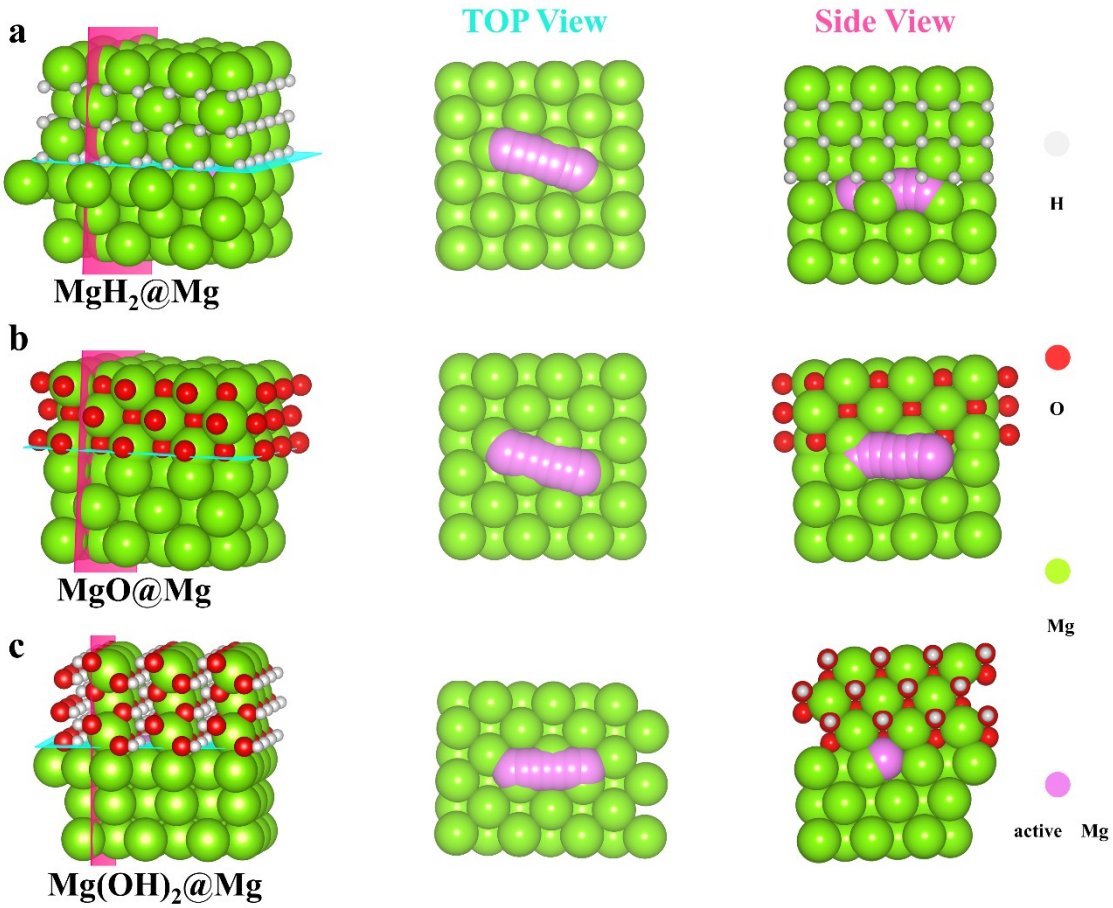

Figure S17. DFT calculations on Mg-atom diffusion barriers across varied interfaces. The diffusion pathways of Mg-atoms at the MgH_2(001)/Mg(0001) interface, MgO(001)/Mg(0001) interface and $Mg(OH)_2$(001)/Mg(0001) interface are simulated and both the top and side views are drawn accordingly.

The energy distributions of Mg-atom along the diffusion path at the MgH_2(001)/Mg(0001), MgO(001)/Mg(0001) and $Mg(OH)_2$(001)/Mg(0001) interfaces have been calculated. The diffusion barriers at the MgO(001)/Mg(0001) and $Mg(OH)_2$(001)/Mg(0001) interfaces are 0.25 eV and 0.33 eV, respectively. These values are higher than 0.19 eV on MgH_2(001)/Mg(0001) interface. The lower diffusion barrier suggests that the MgH_2 formation is favorable for the Mg ions diffusion during repeated Mg plating/stripping cycles.

We have employed the Vienna Ab Initio Package (VASP)[8,9] to perform all the density functional theory (DFT) calculations within the generalized gradient approximation (GGA) using the PBE[10] formulation. We have chosen the projected augmented wave (PAW) potentials[11,12] to describe the ionic cores and take valence electrons into account using a plane wave basis set with a kinetic energy cutoff of 520eV. Partial occupancies of the Kohn−Sham orbitals were allowed using the Gaussian smearing method and a width of 0.05 eV. The electronic energy was considered self-consistent when the energy change was smaller than 10^{-5} eV. A geometry optimization was considered convergent when the force change was smaller than 0.05 eV/Å. Grimme's DFT-D3 methodology[13] was used to describe the dispersion interactions. Finally, transition states for elementary reaction steps were determined by the nudged elastic band (NEB) method[14]. In the NEB method, the path between the reactant and product is discretized into a series of structural images.

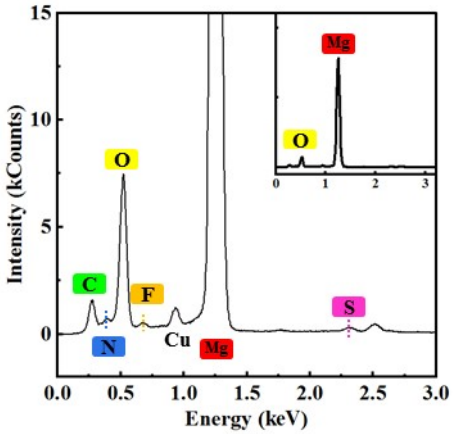

Figure S18. EDS profile of electrodeposits (inset shows the spectrum with complete peak of Mg element to clearly describe the relative content of included elements).

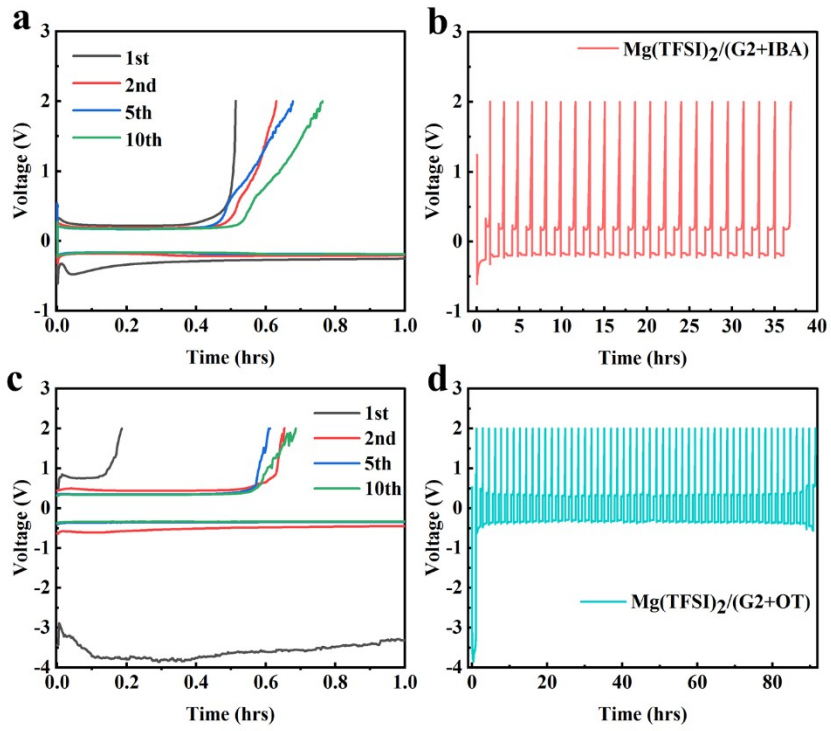

Figure S19. Electrochemical performance of Mg//Cu cells with electrolytes added with primary amine co-solvents. Constant current charge/discharge curves as well as voltage curves of Mg//Cu cells under 0.1 M $Mg(TFSI)_2$/(G2+IBA) (a-b) and $Mg(TFSI)_2$/(G2+OT) (c-d) electrolytes at 0.1 mA cm^{-2}.

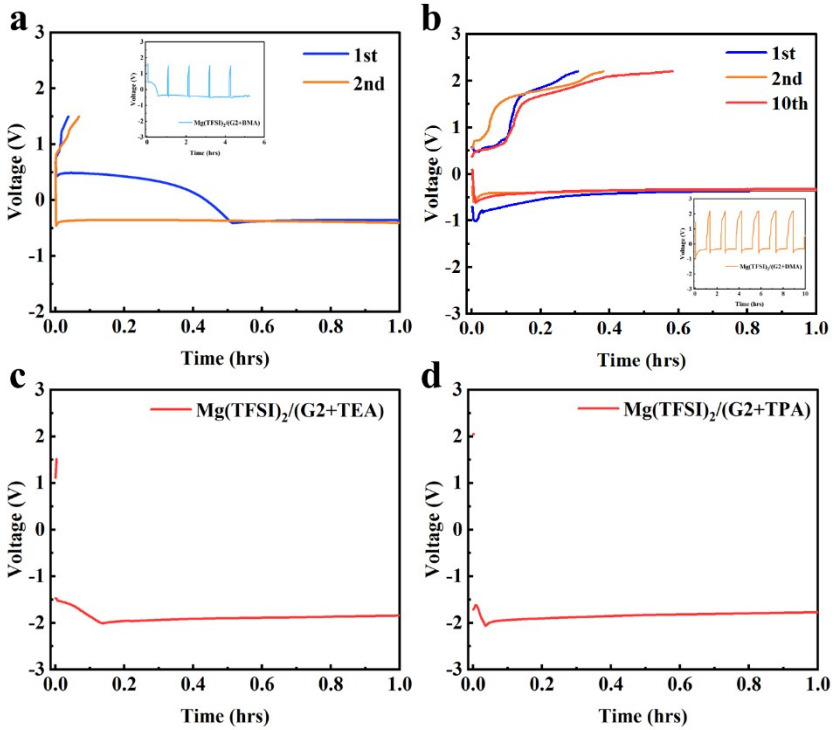

Figure S20. Electrochemical performance of Mg//Cu cells with electrolytes added with secondary and tertiary amine co-solvents. The constant current charge/discharge curves as well as the voltage profiles of the Mg//Cu cell under $Mg(TFSI)_2$/(G2+BMA) (a), $Mg(TFSI)_2$/(G2+DMA) (b), $Mg(TFSI)_2$/(G2+TEA) (c) and $Mg(TFSI)_2$/(G2+TPA) (d) electrolytes were plotted.

The overpotential of Mg//Cu cells during Mg plating/stripping was reduced in the electrolyte with secondary amine co-solvent (Figure S20a-b), while it was not improved in the electrolyte with the addition of tertiary amine co-solvent (Figure S20c-d).

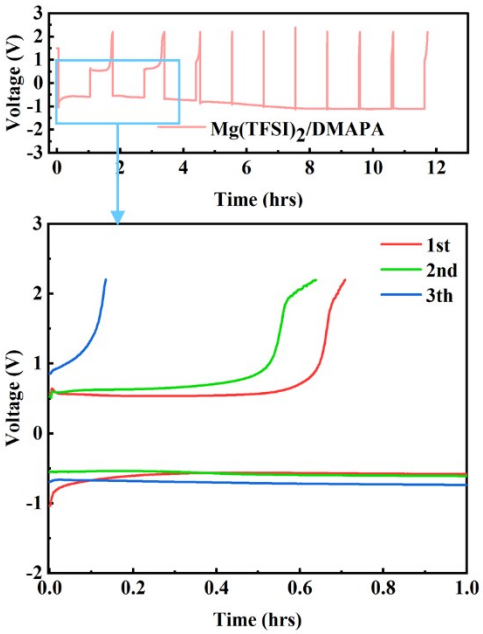

Figure S21. Constant-current charge/discharge curves as well as voltage-current curves of Mg//Cu cells with 0.1 M $Mg(TFSI)_2$/DMAPA electrolyte.

In the case of pure amine reagents as solvents for electrolytes, their electrochemical performance is poor, and although their overpotential is only about 0.5 V in the first two cycles, the Coulombic efficiency decreases sharply after two cycles. This indicates that G2 plays a critical role as a co-solvent in the electrolyte system.

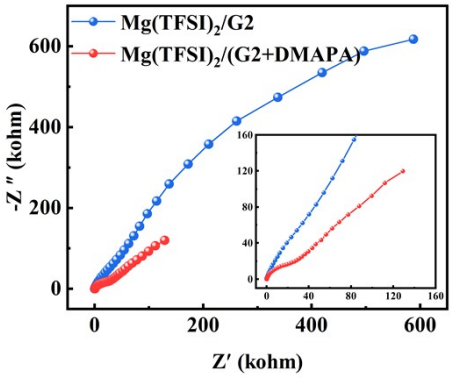

Figure S22. EIS of $Mg(TFSI)_2$/G2 and $Mg(TFSI)_2$/(G2+DMAPA) electrolytes.

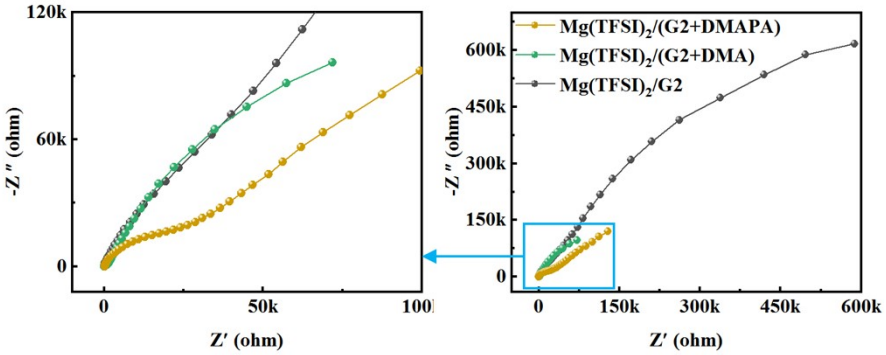

Figure S23. EIS of Mg//Cu cells in various electrolytes.

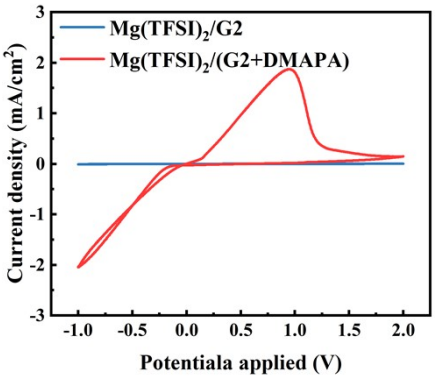

Figure S24. CV curves of $Mg(TFSI)_2$/G2 and $Mg(TFSI)_2$/(G2+DMAPA) electrolytes in Mg//Cu cells.

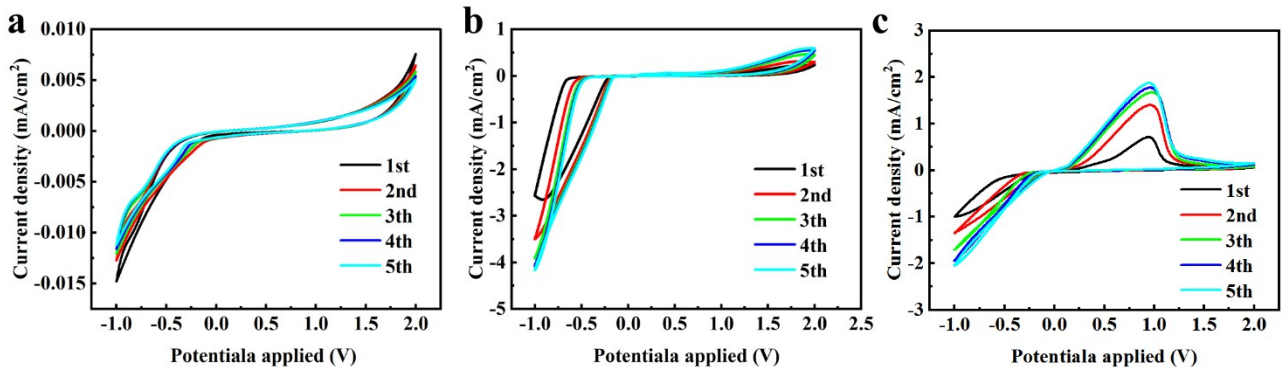

Figure S25. Effects of 0.1 M electrolytes on electrochemical performance of Mg//Cu cells. CV of Mg plating/stripping behavior of Mg//Cu cells in $Mg(TFSI)_2$/G2 (a), $Mg(TFSI)_2$/(G2+DMA) (b), $Mg(TFSI)_2$/(G2+DMAPA) (c) electrolytes at a scan rate of 25 mV s^{-1}.

In the CV curves of Mg//Cu cells using different electrolytes, there is essentially no significant increase in the current response of the $Mg(TFSI)_2$/G2 electrolyte over the voltage range of -1.0 V to 2.0 V as the electrochemical reaction proceeds. And a smaller anodic peak near about 0.4 V can be seen in the $Mg(TFSI)_2$/(G2+DMA) electrolyte, which is consistent with the results of the charge/discharge curves in Figure 5a. Notably, the current response becomes consistently larger in the $Mg(TFSI)_2$/(G2+DMAPA) electrolyte, indicating that this electrolyte has good plating/stripping reversibility in the Mg//Cu cell.

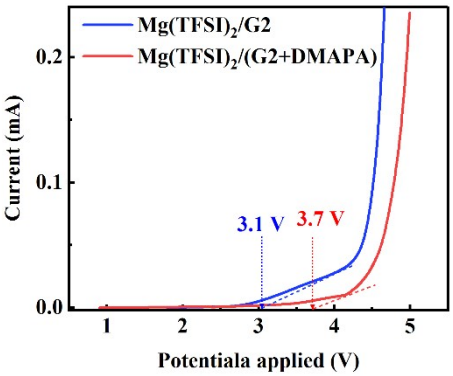

Figure S26. Linear sweep voltammetry (LSV) images of Mg//SS cells (Scan rate of 1 mV s^{-1}).

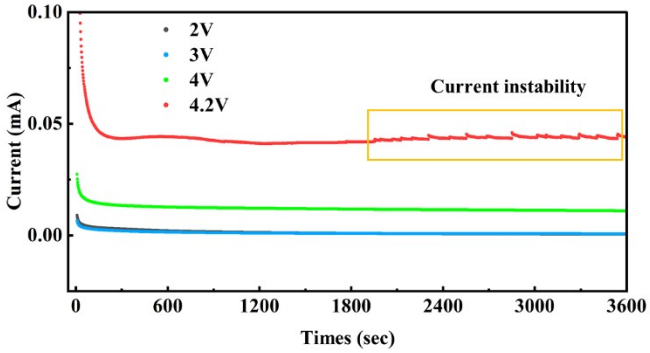

Figure S27. Current-time profiles of $Mg(TFSI)_2$/(G2+DMAPA) electrolyte at different voltages in Mg//SS cells.

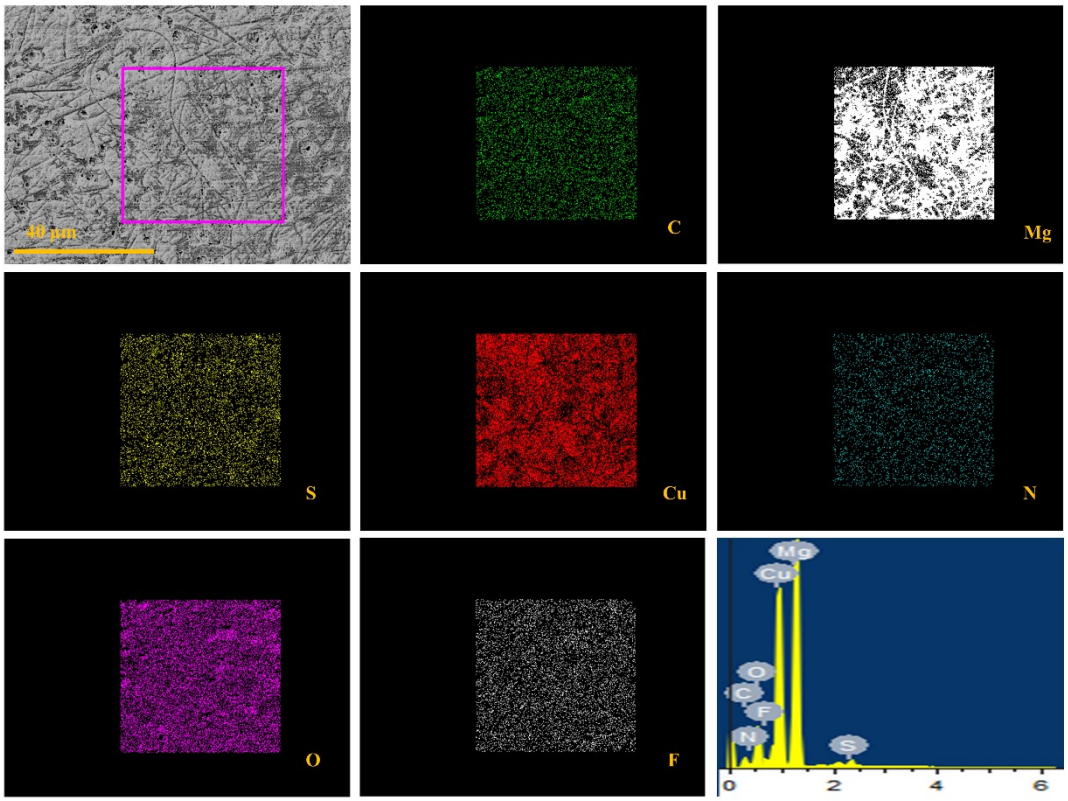

Figure S28. SEM images of Mg//Cu cells in 0.1 M $Mg(TFSI)_2$/(G2+DMAPA) electrolyte (after 9 hours of overcharging) and the corresponding EDS spectra of the various elements (scale bar: 40 µm).

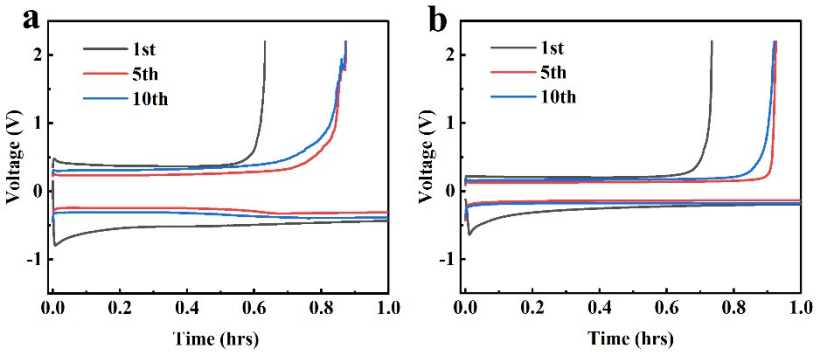

Figure S29. Constant current charge/discharge curves and voltage profiles of Mg//Al (a) and Mg//SS cells (b) under $Mg(TFSI)_2$/(G2+DMAPA) electrolyte.

Table S1. Determination of major bands in the fingerprint region of infrared absorption spectra of DMAPA and G2

Free base vibrational mode	**Wavenumbers (cm^{-1})**
$-NH_2$ symmetric stretching mode	3368
$-NH_2$ antisymmetric stretching mode	3294
$-NH_3^+$stretching mode	2960
C-H stretching	3000-2800
N-H in-plane bend	1596
C-N stretch	1029

Table S2. Detailed single crystal structural information from a 0.1 M $Mg(TFSI)_2$/(G2+DMAPA) electrolyte.

Crystal data and structure refinement of $[Mg(DMAPA)_6][TFSI]_2$	
Chemical formula	$C_{34}H_{85.6}F_{12}MgN_{14}O_8S_4$
Formula weight	1199.299
Temperature(K)	170 K
Crystal system	triclinic
Space group	P -1
Hall group	-P 1
Volume($Å^3$)	3041.0(12)
a (Å)	9.611(2)
b (Å)	15.130(3)
c (Å)	21.533(5)
α(°)	91.969(8)
β(°)	96.720(9)
γ(°)	101.570(9)
$\rho_{calc}g/cm^3$	1.310
Wavelength	0.71073
Z	2
μ/mm^{-1}	0.256
F000	1269.2
Crystal size/mm^3	0.2×0.1×0.1
Independent reflections	13901 [R_{int} = 0.0559, R_{sigma} = 0.0695]
Goodness-of-fit on F^2	Goodness-of-fit on F^2
Final R indexes [I>=2σ (I)]	R_1 = 0.0642, wR_2 = 0.1497
Final R indexes [all data]	R_1 = 0.1101, wR_2 = 0.1786

Table S3. X-ray photoelectron spectrum peak allocation.

Spectrum	Species	Binding Energy (eV)	Ref
Mg 2*p*	Mg	49.70	15
	MgO	50.1-50.8	16
	MgS_x	50.3-50.7	17, 18
	$Mg(OH)_2$	52	16
C 1*s*	-C-C-	284.80	19
	-C-H, -C-O	285-286	20
	-C=O	286.89	20
	O-C=O	288.5	19
	$MgCO_3$	290.18	17
	$-CF_3$	293	21
O 1*s*	MgO	530.92	22, 23
	$Mg(OH)_2$	532	17
	Polyether or -C-O-C	532-533	20
	Polyester or O=C-O-	533.50-534	24
F 1*s*	MgF_2	685-686	25
	$-CF_2$, -CF	686.5-687.5	26
	$-CF_3$ (from $TFSI^-$)	688.2-688.6	27
	$-CF_2-CF_2-$	689.4-690	20
S 2*p*	MgS_x	163-169	28
	$-SO_x$	161.5-163	27
	O=S=O (from $TFSI^-$)	169.40	21
N 1*s*	S-N-S	399.74	21
	-N-S	400.91	21

Table S4. Ionic conductivity of various electrolytes.

Electrolyte	Ionic conductivity (mS cm^{-1})
$Mg(TFSI)_2$/G2	1.32
$Mg(TFSI)_2$/(G2+DMA)	2.80
$Mg(TFSI)_2$/(G2+DMAPA)	1.02

The ionic conductivity of the electrolyte is calculated by the following equation:

$$\sigma = \frac{L}{SR}$$

where σ: ionic conductivity, L: thickness of the diaphragm after being completely infiltrated, S: surface area of the glass fiber, R: resistance value measured by electrochemical impedance spectra.

The ionic conductivity of different electrolytes varied, and the ionic conductivity of $Mg(TFSI)_2$/(G2+DMA) electrolyte was significantly better than that of other electrolytes (~2.8 mS cm^{-1}), indicating that $Mg(TFSI)_2$/(G2+DMA) should have an advantage in the ion transport process in the bulk phase. On the contrary for $Mg(TFSI)_2$/(G2+DMAPA) electrolyte its ability to transport ions is much weaker.

Reference

1. G. J. Xu, J. D. Li, C. Wang, X. F. Du, D. Lu, B. Xie, X. Wang, C. L. Lu, H. S. Liu, S. M. Dong, G. L. Cui and L. Q. Chen, *Angew. Chem., Int. Ed,* 2021, **60**, 7770-7776.
2. B. Delley, *The Journal of Chemical Physics*, 1990, **92**, 508-517.
3. F. J. Devlin, P. J. Stephens, J. R. Cheeseman and M. J. Frisch, *The Journal of Physical Chemistry A*, 1997, **101**, 6322-6333.
4. H. Sun, *The Journal of Physical Chemistry B*, 1998, **102**, 7338-7364.
5. G. W. T. M. J. Frisch, H.B. Schlegel, G.E. Scuseria, M.A. Robb, J.R. Cheeseman, G. Scalmani, V. Barone, G.A. Petersson, H. Nakatsuji, X. Li, M. Caricato, A.V. Marenich, J. Bloino, B.G. Janesko, R. Gomperts, B. Mennucci, D.J. Hratch., 2006.
6. Y.-L. Wang, F. U. Shah, S. Glavatskih, O. N. Antzutkin and A. Laaksonen, *The Journal of Physical Chemistry B*, 2014, **118**, 8711-8723.
7. M. J. Abraham, T. Murtola, R. Schulz, S. Páll, J. C. Smith, B. Hess and E. Lindahl, *SoftwareX*, 2015, **1-2**, 19-25.
8. G. Kresse, J. Furthmüller, *Computational Materials Science*, 1996, **6**, 15-50.
9. G. Kresse, J. Furthmüller, *Phys. Rev. B,* 1996, **54**, 11169−11186.
10. J. P. Perdew, K. Burke, M. Ernzerhof, *Physical Review Letters*, 1996, **77**, 3865-3868.
11. G. Kresse, D. Joubert, *Physical Review B*, 1999, **59**, 1758-1775.
12. P. E. Blöchl, *Physical Review B*, 1994, **50**, 17953-17979.
13. S. Grimme, J. Antony, S. Ehrlich, H. Krieg, *J. Chem. Phys.,* 2010, **132**, 154104.
14. G. Henkelman, B. P. Uberuaga, H. Jonsson, *J. Chem. Phys.* 2000, **113**, 9901.
15. S. Hou, X. Ji, K. Gaskell, P.-f. Wang, L. Wang, J. Xu, R. Sun, O. Borodin and C. Wang, *Science*, 2021, **374**, 172-178.
16. V. Rheinheimer, C. Unluer, J. Liu, S. Ruan, J. Pan and P. J. M. Monteiro, *Journal*, 2017, **10**.
17. V. Fournier, P. Marcus and I. Olefjord, *Surface and Interface Analysis*, 2002, **34**, 494-497.
18. F. Yang, R. Hunger, K. Roodenko, K. Hinrichs, K. Rademann and J. Rappich, *Langmuir*, 2009, **25**, 9313-9318.
19. A. V. Shchukarev and D. V. Korolkov, *Central European Journal of Chemistry*, 2004, **2**, 347-362.
20. *Journal of Chemical Education*, 1993, **70**, A25.
21. R. Dedryvère, S. Leroy, H. Martinez, F. Blanchard, D. Lemordant and D. Gonbeau, *The Journal of Physical Chemistry B*, 2006, **110**, 12986-12992.
22. C. Fotea, J. Callaway and M. R. Alexander, *Surface and Interface Analysis*, 2006, **38**, 1363-1371.
23. M. Estrada, V. V. Costa, S. Beloshapkin, S. Fuentes, E. Stoyanov, E. V. Gusevskaya and A. Simakov, *Applied Catalysis A: General*, 2014, **473**, 96-103.
24. G. P. NatureAngewandte Chemie International Edition in EnglishLópez, D. G. Castner and B. D. Ratner, *Surface and Interface Analysis*, 1991, **17**, 267-272.
25. S. Mertin, L. Marot, C. S. Sandu, R. Steiner, J.-L. Scartezzini and P. Muralt, *Adv. Eng. Mater.*, 2015, **17**, 1652-1659.
26. M. I. Nandasiri, L. E. Camacho-Forero, A. M. Schwarz, V. Shutthanandan, S. Thevuthasan, P. B. Balbuena, K. T. Mueller and V. Murugesan, *Chem. Mater.*, 2017, **29**, 4728-4737.
27. L. Suo, O. Borodin, T. Gao, M. Olguin, J. Ho, X. Fan, C. Luo, C. Wang and K. Xu, *Science*, 2015, **350**, 938-943.
28. T. Gao, S. Hou, K. Huynh, F. Wang, N. Eidson, X. Fan, F. Han, C. Luo, M. Mao, X. Li and C. Wang, *ACS Appl. Mater. Interfaces*, 2018, **10**, 14767-14776.